




Article

Small Angle Scattering Intensity Measurement by an Improved Ocean Scheimpflug Lidar System

Hongwei Zhang¹, Yuanshuai Zhang¹, Ziwang Li¹, Bingyi Liu^{1,2}, Bin Yin¹ and Songhua Wu^{1,2,3,*} 

¹ Department of Marine Technology, College of Information Science and Engineering, Ocean University of China, Qingdao 266100, China; zhanghongwei8944@ouc.edu.cn (H.Z.); zhangys01@aircas.ac.cn (Y.Z.); liziwang@stu.ouc.edu.cn (Z.L.); liubingyi@ouc.edu.cn (B.L.); binyin@ouc.edu.cn (B.Y.)

² Laboratory for Regional Oceanography and Numerical Modeling, Pilot National Laboratory for Marine Science and Technology (Qingdao), Qingdao 266200, China

³ Institute for Advanced Ocean Study, Ocean University of China, Qingdao 266100, China

* Correspondence: wush@ouc.edu.cn; Tel.: +86-532-66782573

Abstract: Quantification of the horizontal patterns of phytoplankton and the distribution of suspended particles across the sea's surface has been greatly improved by traditional passive oceanic color remote sensing technology. Lidar technology has already been proven to be effective positive remote sensing technology to construct high-resolution bathymetry models. Lidar technology significantly improves our ability to model biogeochemical processes in the upper ocean and provides advanced concepts regarding the vertical distribution of suspended particles and oceanic optical properties. In this paper, we present a novel optical approach to measuring the scattering intensity and characteristics of suspended particles within small angles backwards and distinguish water medium with different attenuation coefficients by a laboratory demonstration of the ocean Scheimpflug lidar system. The approach allows the direct determination of the scattering intensity over a small angle at the backward direction (175.8~178.8°) with an angular resolution of 0.38. Corrections for the effects of refraction at the air-glass-water interface were demonstrated. The data production (initial width and width attenuation rate of the laser beam) of the ocean Scheimpflug lidar system were utilized to distinguish water with different algae concentrations. Application for the measurement of backward scattering intensity and laser beam width were explored in distances up to several meters with spatial resolutions of millimeter precision.

Keywords: lidar; remote sensing sensors; backward scattering intensity; ocean Scheimpflug lidar; volume scattering function



Citation: Zhang, H.; Zhang, Y.; Li, Z.; Liu, B.; Yin, B.; Wu, S. Small Angle Scattering Intensity Measurement by an Improved Ocean Scheimpflug Lidar System. *Remote Sens.* **2021**, *13*, 2390. <https://doi.org/10.3390/rs13122390>

Academic Editors: Chung-Ru Ho, Antony K. Liu and Xiaofeng Li

Received: 13 April 2021

Accepted: 17 June 2021

Published: 18 June 2021

Publisher's Note: MDPI stays neutral with regard to jurisdictional claims in published maps and institutional affiliations.



Copyright: © 2021 by the authors. Licensee MDPI, Basel, Switzerland. This article is an open access article distributed under the terms and conditions of the Creative Commons Attribution (CC BY) license (<https://creativecommons.org/licenses/by/4.0/>).

1. Introduction

Researchers are able to study large-scale horizontal patterns of phytoplankton and the distribution of suspended particles across the sea's surface and no longer want to just observe the ocean for short periods in small places, spurred by advances in spaced platforms, air-ground telecommunications, and marine detection technology [1–3]. In terms of ocean color remote sensing, optical properties and the distribution of particles are key parameters for estimating upper ocean primary production and for quantifying the spatial distributions of specific constituent concentrations from satellites [3,4]. Inherent optical properties (IOPs, including the volume scattering function (VSF) and the absorption coefficient) of aquatic medium play vital roles in optical oceanography. Remote sensing of water constituents based on traditional ocean color remote sensing technology are determined by the light field underwater [5]. Improvements in ocean color observations, the distribution of particles, and the visibility of water are benefit from the study of these optical properties, especially the measurement of the backward scattering coefficient b_b [6,7].

The dynamic range of VSF variability and the true value of the absorption coefficient in the ocean are little known, largely due to the practical difficulty in carrying out the direct measurement of these parameters [8]. Researchers must apply radiative transfer models to study the property of suspended particles. Current radiative transfer models, which were created more than 40 years ago, are based on a limited set with coarsely resolved angular distribution of scattering intensity [9,10]. Furthermore, the nature properties of the suspended particulate matter in the oceans can be retrieved from the study of the ocean water VSF [11].

Commercial instruments have been widely used for the in situ measurement of water's optical properties and the validation of the remote sensing data, e.g., Laser In Situ Scattering and Transmissometer (LISST), HydroScat Optical Backscattering Sensor (HydroScat-6), and Environmental Characterization Optics (ECO) [12–14]. All these devices are able to measure scattering at a few fixed angles or measure scattering intensity over a narrow range in the forward direction under manual operation. In terms of these point measurement devices, the shipborne platform is the only reliable platform to carry out the observation of oceanic water properties with a large demand for labor.

Lidar technology has already proven to be effective positive remote sensing technology that produces high-resolution models of bathymetry [15]. Lidar technology significantly improves our ability to model biogeochemical processes in the upper ocean and provides advanced conceptions about the vertical distribution of suspended particles and oceanic optical properties [16,17].

The predominant positive remote sensing technology for atmospheric and aquatic applications are based on the time-of-flight method by utilizing pulsed lasers, which have been widely used in the observation of atmospheric constituents such as aerosols, molecules, and meteorological parameters including temperature and wind [18–21]. In the manufacture of a Scheimpflug lidar, a high-power continuous-wave (CW) laser rather than a pulsed laser is utilized. In terms of traditional pulsed lidar systems, the spatial resolution is determined by the width of laser pulses, calculated by the time-of-flight method. The range resolution of a Scheimpflug lidar system is achieved through a triangulation method [22–24]. With further research and exploration of the Scheimpflug lidar, the application fields of the Scheimpflug lidar cover spectroscopy techniques for entomological applications based on elastic and inelastic lidar [25–28], remote sensing of atmospheric aerosol and particles by utilizing multi-channel Raman lidar [29], gas monitors by performing differential absorption lidar [30,31], and the detection of aquatic and vegetation by operating the hyperspectral lidar [26,32].

Gordon studied the influence of multiple scattering on the optical characteristics of sea water detected by marine lidar [33]. Walker formulated entirely analytical lidar equations for a turbid water medium that included beam spreading and pulse stretching. The lidar equations were reduced to simple algorithms which served as useful engineering models for systems study by accompany the lidar equations with simplified approximations [34]. Roddewig derived the diffuse attenuation coefficient of downwelling irradiance (K_d) in Yellow Lake by analyzing two sets of airborne lidar data. Reddewig compared the calculated lidar K_d values with the eight-day-averaged K_d measurement retrieved by the moderate resolution imaging spectrometer (MODIS) and converted the K_d measurements to the Secchi disk depth [35].

Spurred by the old Scheimpflug principle, a novel and compact 2D Ocean Scheimpflug lidar system was developed for the profile measurements of water medium based on the Scheimpflug lidar system to distinguish water medium with a different attenuation coefficient. The Scheimpflug lidar presented in this paper is a laboratory demonstration system. The effective measurement range was 1.31–4.54 m with a spatial resolution of 0.36–4.8 mm. The backward scattering angles varied from 175.5 to 178.8°, the angular resolution was from 72 mrad to 80.8 mrad. The future Scheimpflug lidar system will be packaged in compact housing and configured to the research ship (Dongfanghong-3, which is affiliated with the Ocean University of China) to carry out long-term observation of

water properties over a large sea area (300 sailing days/year; coverage area: northwest Pacific Ocean, Yellow Sea, Indian Ocean). When applied to the field ocean observation, the measurement range of the Scheimpflug lidar system can be modified to profile the optical parameters of ocean water from 2 to 30 m in depth.

The general principle and detailed specification of the ocean Scheimpflug lidar system are introduced in Section 2. The methodology for data processing and the Monte Carlo simulation are described in Section 3 to provide a detailed explanation of the processing of the data production and the validation data. Measurement data and validation data are described in detail in Section 4. Section 5 presents the discussion and conclusion of the laboratory experiment and data analysis.

2. The Ocean Scheimpflug Lidar System

2.1. General Principle

The Scheimpflug lidar system is a novel lidar system based on the Scheimpflug principle. The Scheimpflug principle states that in a scenario with infinite focal depth, to satisfy the Scheimpflug principle, the object plane, the lens plane, and image plane should be interested in the same point. In this scenario, there is no relationship between the focal depth and the optical aperture of the optical system. Figure 1 illustrates a typical Scheimpflug lidar system that has a lens (lens plane) and object planes that are not parallel, and three points (i.e., the image plane, object plane, and the lens plane) intersect at the Scheimpflug intersection point. The backscattering echo signal can be collected by the lens and detected by the tilted 2D CMOS sensors when a laser beam transmits into the water media. In a Scheimpflug lidar system, CMOS pixels correspond with the illuminated volume. Continuous-wave laser sources are common light sources that have been widely employed for range-resolved measurements using the Scheimpflug principle. All the configurations of the Scheimpflug lidar system significantly reduce the cost and the system complexity and differ from conventional lidar systems by utilizing the pulsed light.

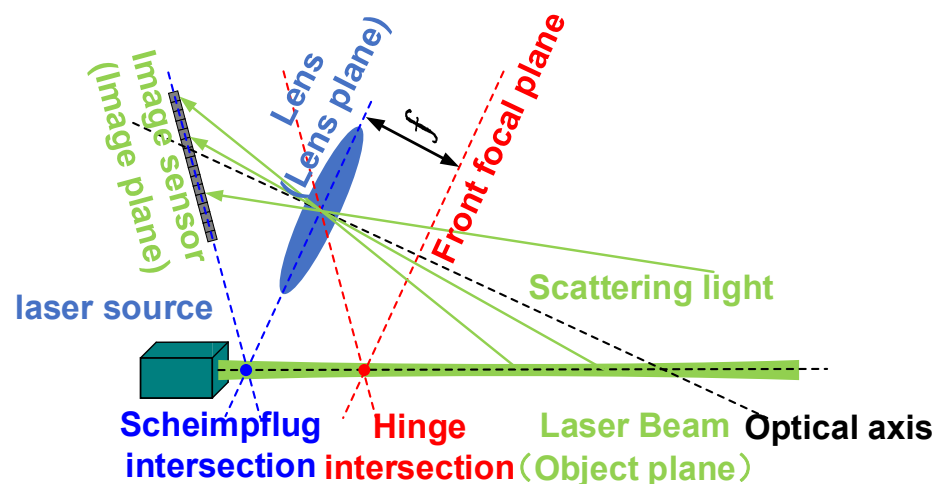


Figure 1. Scheme diagram of the Scheimpflug imaging principle.

2.2. Specifications of the Scheimpflug Lidar System

A typical lidar system includes a laser transmitting system, a receiving system, and a photoelectric detection system. In this section, detailed specifications of the Scheimpflug lidar system are introduced.

2.2.1. Transmitter

The integration time of the CMOS camera is short, since the output signals of the CMOS camera are easily affected by the radiant power fluctuations of a laser over a short period of time. The light source of the ocean Scheimpflug lidar system was a dual

wavelength DPSS laser operating at 491 and 532 nm with an average energy of 50 mW at each wavelength (Cobolt Calypso 04-01, Cobolt Inc., Solna, Sweden). The laser had a very low intensity noise, achieved by running a single frequency to alleviate competing modes and subsequent mode beating. The coherence length of the laser utilized in the Scheimpflug lidar was typically over 100 m.

2.2.2. Receiver

According to the Scheimpflug principle, it is difficult to determine the focal length of the lens. To obtain the focus length of the lens, the Hinge rule was introduced into the design of the lidar system. According to the Hinge rule, there should be another intersection in which the image plane is displaced to the effective center of the lens, and the front focal plane of the lens and the object plane will coincide. In terms of a typical Scheimpflug lidar system, the laser beam transfer in the water medium is the “object plane”, the telescope is the “imaging lens” and the “image plane” is typically a square CMOS array detector. Details of the geometrical relations between the Scheimpflug principle and Hinge rule is illustrated in Figure 1.

The backscattering light was collected by a 25.4 mm plane convex glass with a focus length of 10 cm. The DPSS laser operated at 532 nm with a narrow bandwidth of less than 1 MHz. To suppress the background radiation, such as fluorescence excited by transmitted laser and possible multi-scattering sunlight, a 532 nm interference filter (FL532-3, Thorlabs Inc., Newton, NJ, USA) with a 3 nm full-width at half maximum (FWHM) was utilized in the Scheimpflug lidar system. The CMOS sensor was mounted at 45°, tilted to the glass plane to satisfy the Scheimpflug principle.

2.2.3. Detector

The imaging detector utilized in this system is a 5 Megapixel Monochrome CMOS sensor (CS505MU, Thorlabs Inc., Newton, NJ, USA) with extremely low noise (<2.5 e⁻ RMS Read Noise) and high sensitivity. The CMOS was packaged by compact housing to provide passive thermal management. The global shutter scans the entire field of view simultaneously, allowing for imaging of fast-moving objects. These features make it ideal for low-light imaging applications. The size of the monochrome CMOS sensor was 2448 × 2048 pixels (approximately 5.0 megapixel, pixel size: 3.54 μm × 3.54 μm). The quantum efficiency was approximately 72%, over 525–580 nm. A polarizer was configured in front of the lens making it only receive the co-polarized echo signal. The FOV of the Scheimpflug lidar system was 35.4 μrad.

3. Experiment and Methodology

3.1. Experimental Setup

The configuration of the ocean Scheimpflug lidar system during the laboratory measurements of the water attenuation coefficient is illustrated in Figure 2. The imaging detector and telescope were configured by fulfilling the Scheimpflug principle and the Hinge rule. A black plastic tank with a 90 mm diameter glass window on its side was filled with water. The distance from the ocean Scheimpflug lidar system to the water-filled tank was approximately 1.3 m. The ocean Scheimpflug lidar system was mounted to make sure the laser beam was perpendicular to the surface of the tank. When the laser illuminated a cross-section of an object in the water, a photo of the echo signal could be obtained on the CMOS camera.

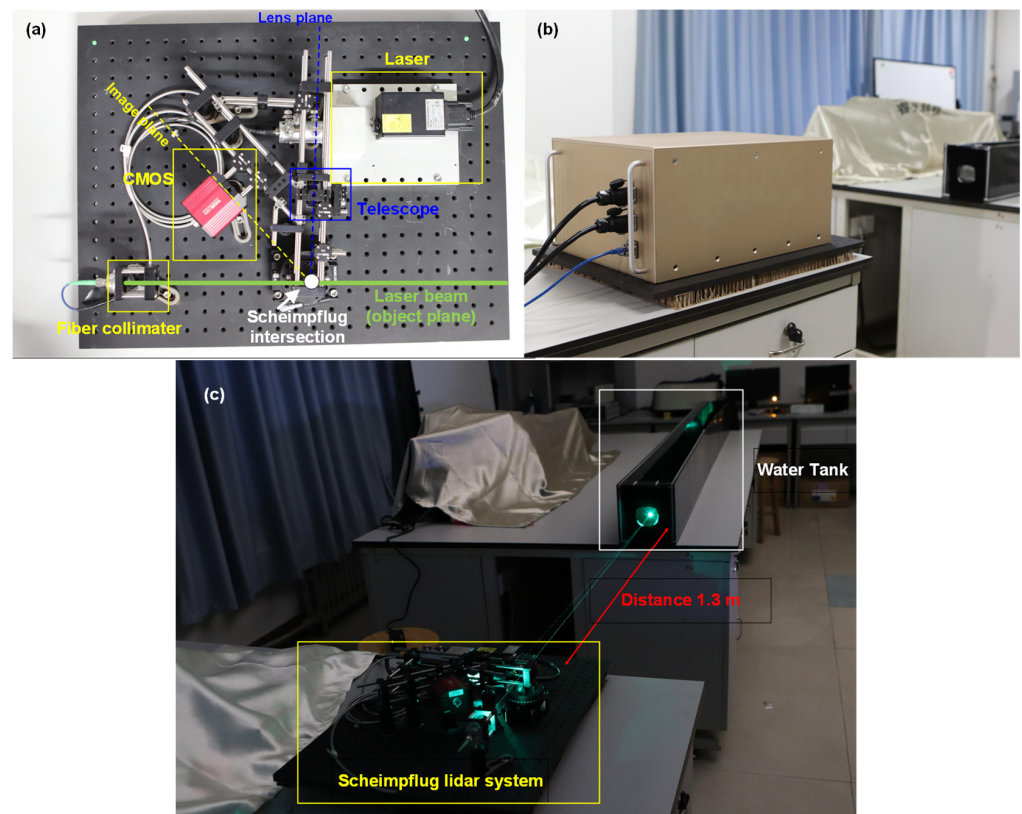


Figure 2. Configuration of the ocean Scheimpflug lidar system during the laboratory measurements of the water attenuation coefficient: (a) top view of the Scheimpflug lidar system; (b) overall appearance of the Scheimpflug lidar system; (c) configuration of the laboratory measurement campaign.

The laser beam was collimated using an achromatic fiber collimator (PAF2-7A, Thorlabs Inc., Newton, NJ, USA) before it was transmitted into the air and a 1.3 m long tank filled with water medium (the collimator was unable to collimate the laser beam to a parallel light strictly. The waist of the laser beam as focused at approximately 5 m away from the collimator. Thus, the laser beam of the Scheimpflug lidar system converged within the measurement range). The telescope in this system is an imaging lens with a diameter of 25.4 mm and a focus length of 100 mm (LB1676-A, Thorlabs Inc., Newton, NJ, USA). The distance between the center of the imaging lens and the “object plane” was 0.105 m as shown in the Figure 3. The angle α is the tilt angle between the lens plane and the object plane, and the tilt angle was set to 87° in our lidar system. The tilt angle β of the image plane to the lens plane was set to 45° , while the image plane was 132° off the optical axis. Thus, the laser beam can image onto the detector surface with a 48° tilt angle off the optical axis. The range calibration and the range correction were performed using Equation (1) as illustrated in Figure 3.

$$Z = \frac{L[D(\sin \beta - \cos \beta \tan \theta) + L']}{D(\cos \beta + \sin \beta \tan \theta) + L' \tan \theta} \quad (1)$$

where $L' = L \tan \beta / \cos \theta$. f is the focal length of the receiving telescope, L is the distance of the center of the image plane to the lens plane, β is the tilt angle of the image plane to the lens plane, and θ is the intersection angle between the scattering light and the laser beam. The focal length of the receiving telescope can be obtained by Equation (2) which is fulfilled with the Hinge rule.

$$f = \frac{L \tan \beta}{\tan \beta \sin \theta + \cos \theta} \quad (2)$$

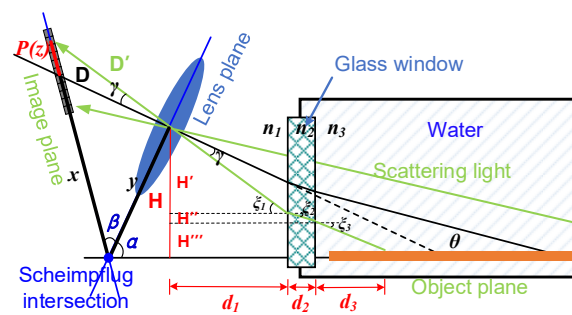


Figure 3. The scheme diagram of the measurement range correction.

In terms of the ocean Scheimpflug lidar system during the experimental measurements, the emitted laser beam and scattering light travelled through at least two interfaces (the interface between the water and glass window and the interface between the glass window and air). The actual distance was no longer consistent with the theoretical distance as Figure 3 illustrated.

For the convenience of system adjustment, a black board was placed in the tank to terminate the beam and to increase the intensity of backscattering echo. In the calibration campaign, fifteen distinct distances were chosen to validate the distance accuracy of the Scheimpflug lidar system. The backscattering echo from the hard target was calibrated to measure the relationship between pixels' position on the CMOS camera and distances, and it is possible to deduce the other distances from the corresponding pixel number (details in the Appendix A). The curves illustrated in Figure 4 depict a theoretical relationship between pixel number and distance. The red curve is the data without taking the glass window into consideration, and the blue curve is the calibrated data. The black dots are experimental test data, which coincide well with the theoretical curve. It can be concluded from the Figure 4 that the distance range of the Scheimpflug lidar system is approximately 1.40–2.80 m. The average range resolution is approximately 1 mm at 1–3 m. The range resolution is determined by the focal length and the tilt angles. Thus, the parameters of the Scheimpflug lidar system should be considered according to specific applications.

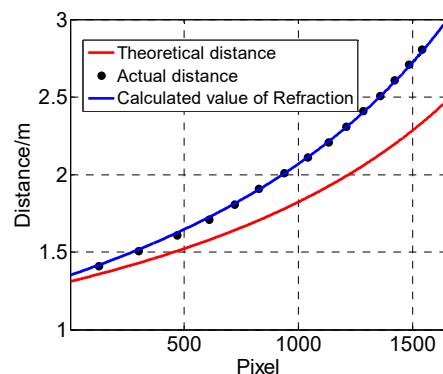


Figure 4. Relationship of the pixel and measurement distance.

3.2. Imaging Processing

During the configuration of a Scheimpflug lidar system, the divergences of the laser beam should be minimized to promise the range resolution and effective range distance. Mei L et al. discussed the importance of divergences of the transmitted laser beam to the atmospheric Scheimpflug lidar [25]. In our setup, the measurement range of the ocean Scheimpflug lidar system is limited to 4.54 m, and it is possible to achieve minimized divergence of the transmitted laser beam by aligning an achromatic fiber collimator (PAF2-7A, Thorlabs Inc., Newton, NJ, USA).

The image width in different distances (pixel) can be obtained by finding the $1/e$ maximum along vertical pixels as illustrated by the white, solid lines in Figure 5a. Part of the data of the CMOS imaging sensor (each square represents a CMOS pixel with 12 bits ADC resolution) are selected for fitting with a Gaussian curve. The laser beam width mentioned in this manuscript is different from the whole halo in a scattering medium due to the multiple scattering process. The traditional definition of the laser beam width is the whole width at transversal direction including the laser beam defined in this manuscript and the halo around the laser beam (the halo width is affected by the sensitivity of detector). The beam width at a related distance can be obtained by finding the $1/e$ maximum intensity value of the Gaussian fitting curve, while the intensity information can be retrieved by finding the maximum intensity value of the fitting curve. By fitting the curves along the laser beam traveling direction, the intensity profile and the beam width profile can be constructed as illustrated in Figure 5c,d.

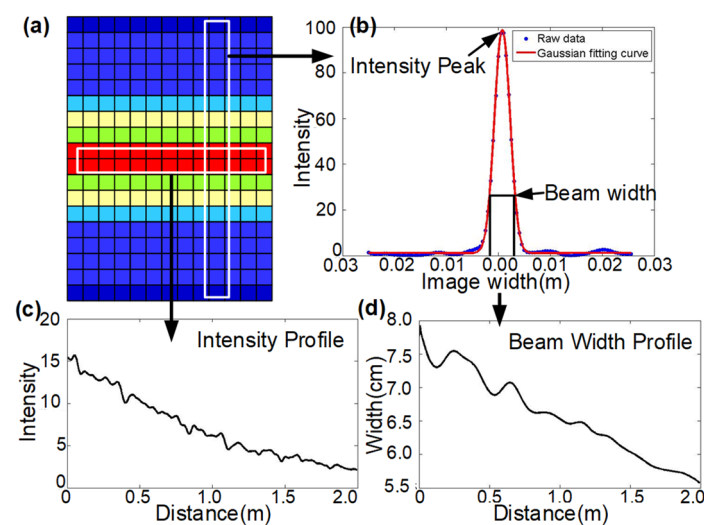


Figure 5. The scheme of the method to retrieve the width of the laser beam from the raw data: (a) part of the data of the CMOS imaging sensor (each square represents a CMOS pixel with 12 bits ADC resolution); (b) the transversal data relative to the laser beam travel direction were extracted to calculate the laser beam width by Gaussian curve fitting; (c) the profile of laser beam intensity which was constructed by collecting all the intensity peaks of the Gaussian curve fitting; (d) the profile of laser's beam width which was constructed by collecting all the beams widths of the Gaussian curve fitting at $1/e$ of intensity peak.

3.3. Monte Carlo Simulation

Monte Carlo simulations have been proven by previous studies to model the probability of different outcomes in a process that cannot easily be predicted due to the intervention of random variables and the accuracy has been verified experimentally. It is a technique that is used to understand the impact of risk and uncertainty in prediction and forecasting models, and it has been widely used to simulate the influence of different lidar measurement modes, different water parameters, and different laser polarization characteristics on photon transmission in seawater [36,37]. The Monte Carlo simulation method can guide the measurement and analysis of field experiments and can well show the distribution characteristics of laser light under water under different water optical characteristics. In this paper, the Monte Carlo simulation method was used to simulate the detection of water bodies to verify the measurement results of this lidar.

The laser beam was set perpendicular to the water's surface, and the photons scattered after colliding with the water medium. During simulation, the position of the photon should be confirmed first to see whether it is involved in the receiving field. If the photon is not involved in the receiving field, it will not track the path of the photon sequentially. Oth-

erwise, the photon scattering path and the scattering points to the detector are determined according to the law of refraction, and then the energy directly scattered into the receiver will be calculated according to the analytical probability. The remaining photons within the FOV will continue to scatter. The analytical probability of the Monte Carlo method can be expressed as:

$$P(z) = \beta(\theta, z) \frac{A}{n^2(h + d/n)^2} \exp[-c(z)d] T_{atm} T_{water} w(z) \quad (3)$$

where A represents the area of the FOV at the water's surface, h represents the distance from detector's surface to the water's surface, d is the depth of the scattering photon within the water medium, $\beta(\theta, z)$ is the volume scattering function at the water depth z , $c(z)$ and $w(z)$ are the attenuation coefficient and weight coefficient of the seawater at depth z , respectively. T_{atm} and T_{water} are the Fresnel transmittance of the atmosphere and water, respectively. $w(0) = 1$, and $w_{n+1}(z) = w_n(z)w_0(z)$ where n and $n + 1$ are the n times and $n + 1$ times scattering [38].

Due to the differences in the attenuation and scattering properties, the multiple scattering processes vary sharply when the laser beam transmits in different water medium, which affects the lidar echo signal. Based on Walker and McLean models, Howard Gordon model, and ocean lidar equations, semi-analytical Monte Carlo simulation methods were used to analyze the effects of lidar observation modes on lidar echo signals, and the relationship between the lidar extinction coefficient α and seawater optical parameters was established [38,39].

Stokes, Mueller, and Meridian methods are typical methods to establish a polarized Monte Carlo simulation model for the radiative transmission of polarized lasers in water, and the model method was used to simulate the process of polarized laser radiation transmission in the sea under typical water conditions to analyze the polarization state of light.

When the polarized light collides with particles, the scattering angle and azimuth angle were obtained through a combination of the Stokes parameter and Mueller matrix. The Stokes parameter was used to characterize the polarization characteristics, while the Mueller matrix was used to characterize the change in polarization state and form a 4×4 phase function matrix. The Stokes parameter $S = [S_0 \ S_1 \ S_2 \ S_3]^T$ was used to describe the polarization state of the laser, S_0 was the light intensity information, S_1 and S_2 were the linearly polarized light components in the x -axis and 45° directions, and S_3 was the circularly polarized light component. The meridional plane of the incident Stokes parameter was defined as the x - z plane, that is, the azimuth was 0. Assuming that the incident light was linearly polarized, the Stokes parameter was $S = [1 \ 1 \ 0 \ 0]^T$. The polarization characteristics were simulated by the Stokes parameter. The polarization scattering phase function (probability density function) composed of the azimuth angle θ and φ can be expressed as:

$$f(\theta, \varphi) = M_{11}(\theta) + M_{12}(\theta)[S_1 \cos(2\varphi) + S_2 \sin(2\varphi)]/S_0 \quad (4)$$

$$M(\theta) = \begin{bmatrix} M_{11}(\theta) & M_{12}(\theta) & 0 & 0 \\ M_{12}(\theta) & M_{11}(\theta) & 0 & 0 \\ 0 & 0 & M_{33}(\theta) & M_{34}(\theta) \\ 0 & 0 & -M_{34}(\theta) & M_{33}(\theta) \end{bmatrix} \quad (5)$$

$M(\theta)$ is the Mueller matrix of the spherical particle, when the radius of the scattering spheres in the scattering medium is small (in the case of Rayleigh scattering). In the case of Rayleigh scattering, the elements in $M(\theta)$ can be expressed as:

$$\begin{aligned} M_{11}(\theta) &= \frac{3}{16\pi} (\cos^2 \theta + 1) \\ M_{12}(\theta) &= \frac{3}{16\pi} (\cos^2 \theta - 1) \\ M_{33}(\theta) &= \frac{3}{8\pi} \cos \theta \\ M_{34}(\theta) &= 0 \end{aligned} \quad (6)$$

The cumulative distribution function of the scattering angle θ can be expressed as:

$$P(0 \leq \vartheta \leq \theta) = 2\pi \int_0^\theta M_{11}(\vartheta) \sin \vartheta d\vartheta = \zeta \quad (7)$$

The scattering angle θ can be solved by the above formula, where ζ is a random number uniformly distributed from 0 to 1. The cumulative distribution function of azimuth ϕ can be expressed by the following formula:

$$\begin{aligned} P(0 \leq \phi \leq \varphi) &= \frac{\int_0^\varphi \left[1 + \frac{M_{12}(\theta)}{M_{11}(\theta)} \frac{S_1 \cos(2\phi) + S_2 \sin(2\phi)}{S_0} \right] d\phi}{\int_0^{2\pi} \left[1 + \frac{M_{12}(\theta)}{M_{11}(\theta)} \frac{S_1 \cos(2\phi) + S_2 \sin(2\phi)}{S_0} \right] d\phi} \\ &= \frac{1}{2\pi} \left[\varphi + \frac{M_{12}(\theta)}{M_{11}(\theta)} \frac{S_1 \cos(2\phi) + S_2 \sin(2\phi)}{S_0} \right] = \zeta \end{aligned} \quad (8)$$

In the simulation presented in this manuscript, both the scattering coefficients of pure water and suspended particles were considered. When the laser transmitted into the water medium, the light will be scattered by the water molecules and suspended particles. The scattering coefficient $b(\lambda)$ is defined as the ratio of the scattering energy within per unit length in the medium to the incident energy. The scattering coefficient included the scattering coefficient of pure water $b_{water}(\lambda)$ and the scattering coefficient of particles $b_{particles}(\lambda)$. The scattering coefficient of pure water was based on the model established by Morel in 1997 [40], while the scattering coefficient of plankton was based on the model mentioned by Gordon in 1983 [41]. Petzold established scattering coefficient of three typical sea waters based on in situ measurement data [42].

4. Results

The key feature of the results obtained by the ocean Scheimpflug lidar system was high-range resolve. Objects separated in space can be measured simultaneously with this technique, especially the measurement of water optical parameter profiles with high resolution. To alleviate the influence of laser energy fluctuations in the raw data of ocean Scheimpflug lidar systems, long-term observation campaigns based on three typical water mediums were carried out. The backscattering signal time series profiles of the ocean Scheimpflug lidar system with 10 s exposure time during validation experiments are illustrated in Figure 6. The color in Figure 6 represents the intensity of the echo signal detected by CMOS. The maximum value of the color bar illustrated in Figure 6a was 10, while the maximum value of the color bar depicted in Figure 6b,c was 35. We can conclude that there were no large variations in the output signal of the CMOS camera over long time periods (16 min), and it is not essential to configure a channel for energy monitor when there was no significant impact upon the magnitude of the output signal from the CMOS camera, especially when the integration time of the CMOS camera was short (10 s) during the entire laboratory experiment campaign.

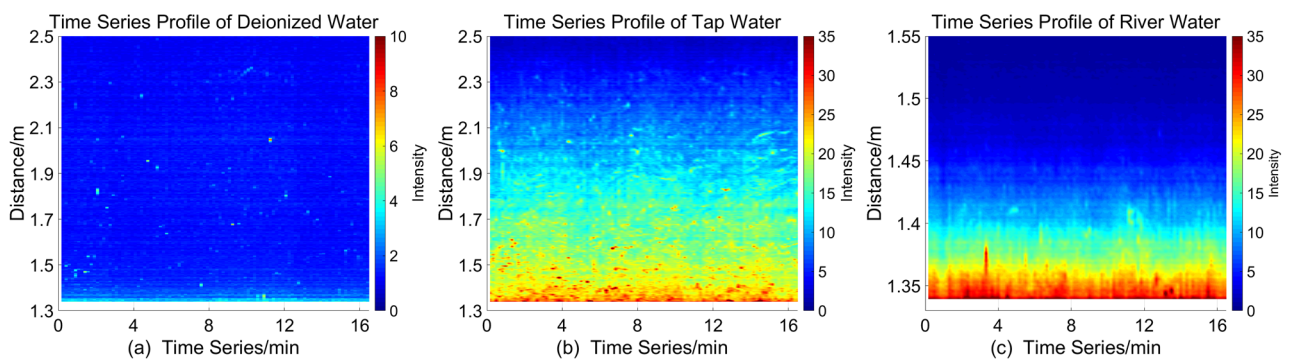


Figure 6. The backscattering signal time series profiles of the ocean Scheimpflug lidar system with 10 s exposure time during validation experiments: (a) the measurement medium was deionized water; (b) the measurement medium was tap water; (c) the measurement medium was river water (the river water samples were taken from the river inside the campus of the Ocean University of China as Figure A2 shows).

Water backscattering images were measured with a 10 s exposure time during nighttime to characterize the profile of the transmitted laser beam under three typical water mediums as shown in Figure 7. The color in Figure 7 represents the intensity of the echo signal detected by CMOS. The maximum value of the color bar illustrated in Figure 7a was 6, while the maximum value of the color bar depicted in Figure 7b,c were 30 and 45, respectively. The echo signal intensity of deionized water was the weakest for the main signal resource, which was the Rayleigh scattering signal of the water molecules as Figure 7a shows. The backscattering images obtained by the ocean Scheimpflug lidar system indicate the intensity of the multi-scattering processing in water medium during the small angle at backward direction. The laser beam could transmit through the whole tank when the measurement medium was tap water as Figure 7b shows. The laser beam could only transmit a short distance when the measurement medium was river water due to the high attenuation coefficient of suspended particles in the river water. From the illustration of Figure 7, we can conclude that the initial width of the laser beam had a maximum value when the medium was river water due to the strong multi-scattering processing. The width of the laser beam obtained by the Scheimpflug lidar system (retrieved by the method mentioned in Section 3.2) decreased slowly, and it transmitted through the whole tank filled with the deionized water. The lidar system performed perfectly when the tank was filled with tap water. The upward curvature in the laser beam width obtained by the Scheimpflug lidar system was the cause of a slight displacement of the CMOS camera, and a detailed analysis can be found in Appendix B.

Width and intensity information of a laser beam can be obtained by utilizing the method mentioned in Section 3.1. Then, the width variation profiles can be constructed by calculating the transversal raw data step by step. Figure 8a,b depict the laser beam width obtained by the Scheimpflug lidar system (retrieved by the method mentioned in Section 3.2) and intensity as a function of distance, respectively. The red lines are the data obtained by the Scheimpflug lidar system when the measurement medium is tap water. The black lines represent the echo signal of river water detected by CMOS. The blue lines depict the changes in the laser beam width obtained by the Scheimpflug lidar system and intensity with distance when the measurement medium is deionized water. The spatial resolution of the Scheimpflug lidar system changed with distance. In Figure 8, data points of the curves were calculated by an averaged 50 raw data points. Figure 8 depicts the laser beam width obtained by the Scheimpflug lidar system (retrieved by the method mentioned in Section 3.2) and intensity as a function of distance. The laser beams could transmit through the whole tank and the laser beam width obtained by Scheimpflug lidar system decreased relatively moderately when the measurement mediums were tap water and deionized water. The laser beam could only transmit a short distance and the laser beam attenuated sharply when the measurement medium was river water due to the

abundance of suspended particles and colored dissolved organic matter (CDOM) in the river water. The width variation profiles of laser beam showed different characteristics under three typical water mediums as Figure 8 shows. The initial width and attenuation rate of laser beams could be effective tools to distinguish water medium with different attenuation coefficient.

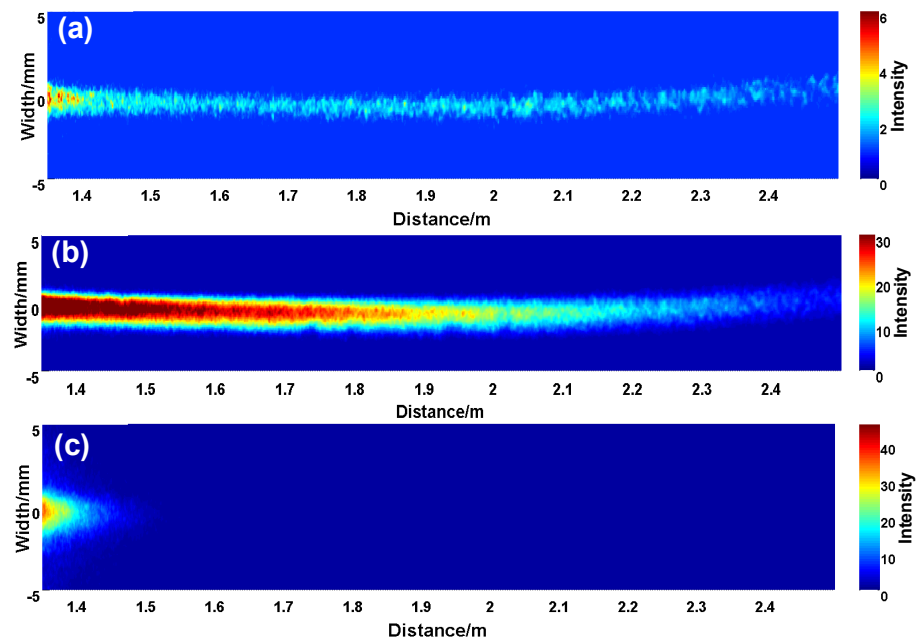


Figure 7. Intensity-range maps under three kinds of water mediums over a 10 s time window with a range interval of approximately 1.32–2.50 m: (a) the intensity-range maps under the measurement medium was deionized water; (b) the intensity-range maps under the measurement medium was tap water; (c) the intensity-range maps under the measurement medium was river water.

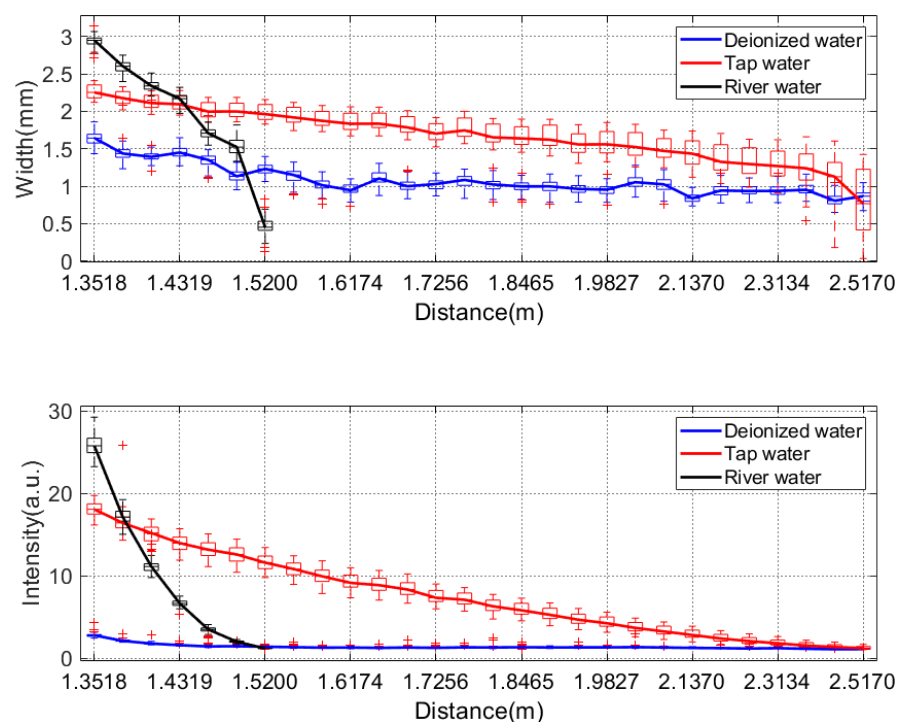


Figure 8. (a) Relationship between the laser beam width and the measurement range. (b) Relationship between the laser beam intensity and the measurement range.

To verify the ability of ocean Schempflug lidar system to distinguish algae at different concentrations by utilizing its data products including the initial width and width attenuation rate of laser beam, three typical algae in China's coastal area (including *Isochrysis galbana*, *Platymonas subcordiformis*, *Nitzschia closterium*) were used during the laboratory observation experiments. The size distributions of the three algae are listed in Table 1. *Isochrysis galbana* are a species of Haptophyta, and are nearly spherical in shape. The size of *Platymonas subcordiformis* and *Nitzschia closterium* are close to long sticks.

Table 1. Size distribution of three typical algae at China coastal area.

Name	Size Distribution (μm)
<i>Isochrysis galbana</i>	Length: 4.4~7.1 Width: 2.7~4.4 Thickness: 2.4~3.0
<i>Platymonas subcordiformis</i>	Length: 11.0~14.0 Width: 7.0~9.0 Thickness: 3.5~5.0
<i>Nitzschia closterium</i>	Length: 12.0~23.0 Width: 2.0~3.0 Thickness: 2.4~3.0

Figure 9 depicts the relationship between initial beam width and beam width attenuation rate obtained by the Schempflug lidar system (retrieved by the method mentioned in Section 3.2) under different mediums. The blue dots represent the data when the measurement medium is *Isochrysis galbana*. The data production of the *Platymonas subcordiformis* was illustrated by the red dots. The initial width information of *Platymonas subcordiformis* are larger than other algae. It is unreliable to distinguish the *Isochrysis galbana* and *Nitzschia closterium* according to the initial width of laser beam. However, it is reliable to distinguish the species of algae by taking both the initial width and attenuation rate into consideration.

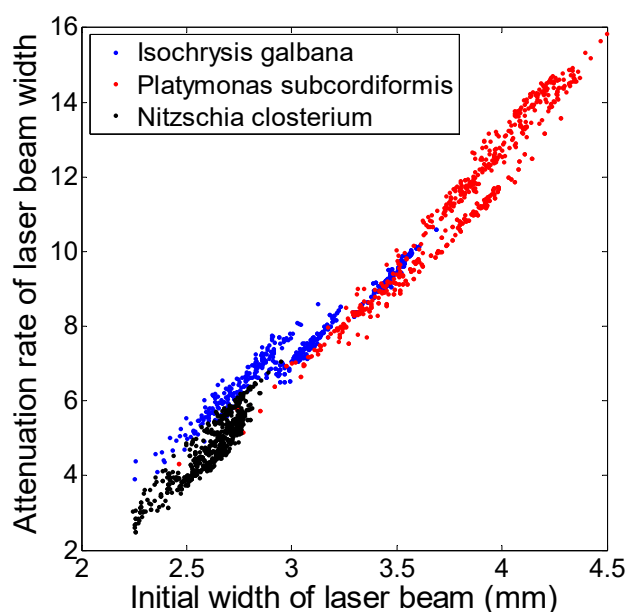


Figure 9. Relationship between the initial beam width and beam width attenuation rate under different medium. The black dots represent the water with *Nitzschia closterium* at different concentrations; the blue dots represent the water with *Isochrysis galbana* at different concentrations; the red dots represent the water with *Platymonas subcordiformis* at different concentrations.

Validation

Monte Carlo simulations have been widely used to simulate the influence of different lidar measurement modes, different water parameters, and different laser polarization characteristics on photon transmission in seawater. The Monte Carlo simulation method utilized in this paper is depicted in Section 3.3 in detail. In this section, the simulated data are illustrated for the validation of Scheimpflug lidar system.

The intensity-range maps simulated by the Monte Carlo method under three water mediums with different attenuation coefficients are illustrated in Figure 10. The color in Figure 10 represents the intensity of the echo signal detected by the CMOS. The maximum value of the color bar illustrated in Figure 10a was 15, while the maximum value of the color bar depicted in Figure 10b,c were 20 and 225, respectively. The intensity-range maps under the measurement mediums with an attenuation coefficient was 0.2 m^{-1} , 0.4 m^{-1} , 2 m^{-1} . From Figure 10, we can find a similar tendency between the simulated data by the Monte Carlo method and the measured data by the Scheimpflug lidar under different water mediums. The laser beam transferred through long distances (up to 4 m) when the attenuation coefficient was 0.2 m^{-1} . The backscattering echo signal within a 2 m measurement range could be detected with an attenuation coefficient that was 0.4 m^{-1} . When the attenuation coefficient was 2 m^{-1} , the maximum distance of the echo signal decreased to 0.375 m. The initial widths of the laser beam illustrated in Figure 10c were broader than the simulation data shown in Figure 10a,b due to the multiple scattering processes varying sharply in different water mediums, which were closely related to the attenuation coefficient.

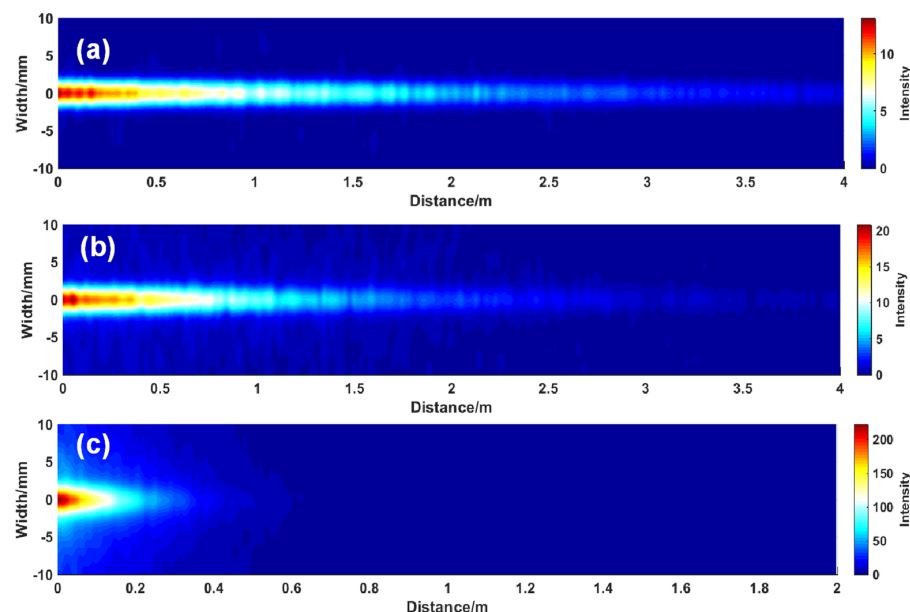


Figure 10. The intensity-range maps simulated by the Monte Carlo method under three different water mediums with different attenuation coefficients: (a) the medium with attenuation coefficient was 0.2 m^{-1} ; (b) the medium with attenuation coefficient was 0.4 m^{-1} ; (c) the medium with attenuation coefficient was 2 m^{-1} .

To quantify the difference of simulated data and measured data, laser beam information (e.g., width and intensity information) were retrieved by the utilized methods mentioned above as Figure 11 shows (the initial width of the measured data were normalized to the simulated data). Figure 11a depicts the changes in laser beams under water medium with different attenuation coefficients. The solid lines (red line represents river water; blue line means tap water; black line depicts deionized water) represent the width information obtained by the Scheimpflug lidar, and the dotted lines (red line represents the attenuation coefficient is 2 m^{-1} ; blue line means the attenuation coefficient is 0.4 m^{-1} ;

black line depicts the attenuation coefficient is 0.2 m^{-1}) mean the data were simulated by the Monte Carlo method. The original absorption coefficient, scattering coefficient, and the attenuation coefficient utilized in this manuscript were obtained from the references as shown in Table 2 [34]. By comparing the simulated data and the measured data, we can conclude that the measured data changed faster with distance than the simulated data, which was mainly due to the attenuation coefficients of the measured medium being larger than the attenuation coefficients during the simulation work. However, there was a singular situation of the width information when the measured medium was tap water. The multi-scattering processing was dominant in the attenuation process rather than the absorption process in the tap water medium (the width of the laser beam obtained by the Scheimpflug lidar system (retrieved by the method mentioned in Section 3.2) indicated the backscattering intensity of the water medium).

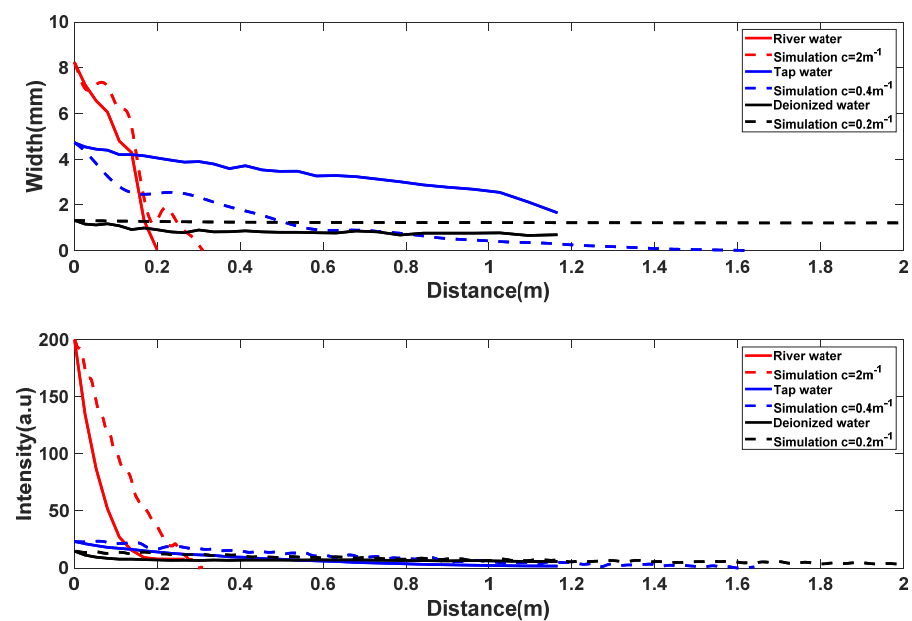


Figure 11. Comparison of measured data obtained by the Scheimpflug lidar and data simulated by the Monte Carlo method: (a) laser beam width (note that the scale is too large to see the small changes in the beam width simulated by the Monte Carlo method when $c = 0.2 \text{ m}^{-1}$); (b) intensity of the laser beam.

Table 2. Water optical properties.

Water Types	a (m^{-1})	b (m^{-1})	c (m^{-1})
Pure sea water	0.0405	0.0025	0.043
Clear sea water	0.114	0.037	0.151
Coastal sea water	0.179	0.219	0.398
Turbid sea water	0.366	1.824	2.190

It is practically difficult to quantify the optical parameters (including the attenuation coefficient, backscattering coefficient, and absorption coefficient) of water medium. The simulated data can only be used for qualitative analysis of the trends in changes of the data. The measured data had good consistency with the simulated data in most cases.

A spectrophotometer has been proven to be good choice to satisfy the demand of precision measurements in the research of organic chemistry, biochemistry, environmental protection, water testing industry, etc. The long optical system inside the spectrophotometer ensures high accuracy and good stability of the instrument. A high-resolution Spectrophotometer (U-3900H, Hitachi Inc., Tokyo, Japan) was operated during the labora-

tory observation experiments to obtain the absorbance that indicates the absorbability of the measured medium to the light, then the absorption coefficient α could be calculated. The GF/FTM filter membrane with a 0.7 μm pore diameter was used to filter the 100 mL measurement medium as shown in Figure 12.

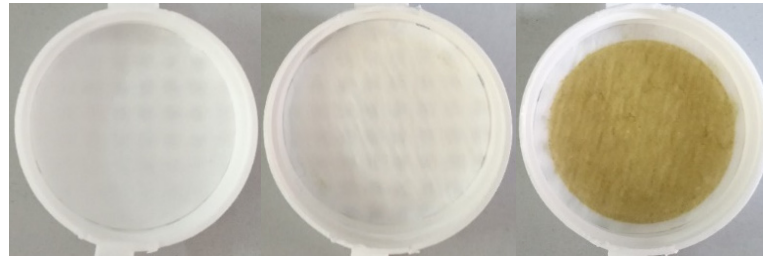


Figure 12. Filter membrane obtained by filtrating three kinds of water bodies.

Results from the data obtained by the spectrophotometer (including the absorbance (blue lines) and absorption coefficient α (red lines)) and the ocean Scheimpflug lidar system (including the attenuation rate of laser beam width (green lines) and attenuation rate of laser beam intensity (black lines)) were illustrated into one figure to study the correlation among the various results as shown in Figure 13. Figure 13a illustrates the variation in the spectrophotometer and ocean Scheimpflug lidar system retrieval results when the water was mixed with different concentration *Nitzschia closterium*. Figure 13b depicts the profiles when the water was mixed with different concentrations of *Isochrysis galbana*. Figure 13c shows the trends in the measurement results with different concentrations of *Platymonas subcordiformis*. As Figure 13 illustrates, the data production of the Scheimpflug lidar system were consistent with the results obtained by the spectrophotometer. By establishing the correspondence between lidar results and spectrophotometer results, the lidar data product can be utilized to obtain the absorption coefficient of the measured medium.

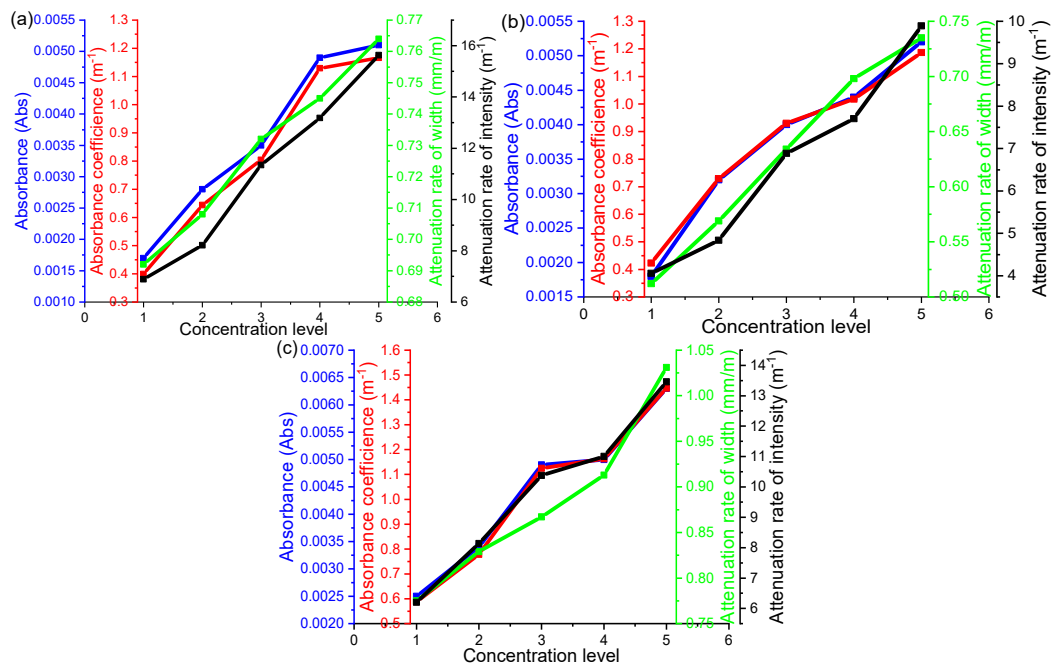


Figure 13. Correlation between the results of spectrophotometer and the data production of the ocean Scheimpflug lidar system: (a) the water with *Nitzschia closterium* at different concentrations; (b) the water with *Isochrysis galbana* at different concentrations; (c) the water with *Platymonas subcordiformis* at different concentrations. Note that the concentration level is defined by adding 100 mL of high concentration algae culture solution into the water tank step by step. The concentrations of algae are relative only.

5. Discussions and Conclusions

In this paper, a laboratory demonstration of the ocean Scheimpflug lidar system was developed with a particular focus on the optical parameters measurement of the aquatic environment. The range resolution of our Scheimpflug lidar system was achieved by utilizing the triangulation method rather than the time-of-flight method commonly used in conventional lidar systems. By positioning the detector, telescope, and the transmitted laser beam in a configuration that fulfills the Scheimpflug principle (in this scene that infinite focal depth can be obtained) and the laser beam can thus be imaged clearly onto the detector.

The conclusions may be summarized as follows:

- A novel optical approach was developed to measure the scattering intensity and to quantify the characteristics of the suspended particles within small angles at backwards and distinguish water medium with different attenuation coefficients.
- The work aimed to verify the capability of the Scheimpflug system to distinguish different water mediums with different optical parameters.
- Intensity-range maps simulated by the Monte Carlo methods under three different water mediums with different attenuation coefficients were developed.

From the carried out experimental verification, we can conclude that the results of improved Scheimpflug lidar system showed good agreement with the theoretical simulation. In all cases, the spatial distribution of the laser beam intensity deduced from the Monte Carlo simulations was found to be very close to the one measured experimentally. The field validation of the Scheimpflug lidar system is the essential work for the future.

In terms of high-precision ocean color remote sensing, IOPs of water medium play a key role in modulating aquatic light field. Unlike the traditional approaches that use a special periscope prism for the measurement of the scattering intensity, the Scheimpflug lidar system allows the direct determination of the VSF over a small angle in the backward direction with high angular resolution. However, the influence of intensity due to the backscattering angles have been ignored in this paper. When it comes to the measurement of VSF, the influence of backscattering angles cannot be ignored.

Polarization lidar systems have been widely utilized in the detection of the distribution of atmospheric aerosols and clouds [21,43]. In a typical polarization-sensitive lidar system, echo signals are easy affected by the scattering particles along the laser beam. In this paper, a polarizer was utilized in the ocean Scheimpflug lidar system to make an echo signal with a single polarized direction. Multi-channels with polarization identification and the size measurement of suspended particles will continue to be researched and developed in subsequent work.

The intensity-range maps simulated by the Monte Carlo method under three different water mediums were slightly different from the data measured experimentally due to the inaccurate settings of the attenuation coefficients.

Author Contributions: Conceptualization, H.Z. and S.W.; Methodology, H.Z., Y.Z. and Z.L.; Validation, H.Z., Y.Z. and B.L.; Formal analysis, H.Z., S.W., Y.Z. and B.L.; Investigation, H.Z.; Data curation, Y.Z. and H.Z.; Writing—original draft preparation, H.Z.; Writing—review and editing, H.Z., S.W., B.L. and B.Y.; Visualization, H.Z., Y.Z. and B.Y.; Supervision, S.W.; Project administration, S.W.; Funding acquisition, S.W. All authors have read and agreed to the published version of the manuscript.

Funding: This research was funded by the National Key Research and Development Program of China under Grant No. 2019YFC1408002 and 2016YFC1400904, and it was supported by the National Natural Science Foundation of China (NSFC) under Grant No. 61975191, U2006217, and 41905022.

Institutional Review Board Statement: Not applicable.

Informed Consent Statement: Not applicable.

Data Availability Statement: The data presented in this study are available on request from the corresponding author.

Acknowledgments: We thank our colleagues for their kind support during the laboratory experiments including Kailin Zhang and Xiangcheng Chen from Ocean University of China for performing the ocean Scheimpflug lidar system and Ke Li and Xiaojuan Kong for the Monte Carlo simulation work.

Conflicts of Interest: The authors declare no conflict of interest.

Appendix A

In a typical ocean Scheimpflug system, the echo signal travels through at least two interfaces (the interface between water and a glass window and the interface between a glass window and air). The specifications of the water Scheimpflug lidar system are fixed including the distance between the center of the CMOS camera and the Scheimpflug intersection x , the distance between the telescope center and the Scheimpflug intersection y , the perpendicular distance between the laser beam and the center of the lens H , the angle between the lens plane and the object plane α , the angle between the lens plane and the plane of CMOS camera β , the distance between the center of the lens and the center of CMOS camera D , the horizontal distance between the center of the lens and the window glass d_1 , and the thickness of the window glass d_2 . The corrected distance d can be derived from the following equation:

$$D' = \sqrt{\left[p(z) + \frac{y}{\cos \beta}\right]^2 + y^2 - 2 \cdot \left[p(z) + \frac{y}{\cos \beta}\right] \cdot y}$$

$$\cos \gamma = \frac{D^2 + D'^2 - p^2(z)}{2 \cdot D \cdot D'}$$

$$\xi_1 = 90^\circ - (\alpha - \gamma)$$

$$H' = d_1 \cdot \tan \xi_1$$

$$\sin \xi_2 = \frac{n_2}{n_1} \sin \xi_1 = \frac{n_2}{n_1} \cos(\alpha - \gamma)$$

$$\sin \xi_3 = \frac{n_3}{n_2} \sin \xi_2 = \frac{n_3}{n_1} \cos(\alpha - \gamma)$$

$$H'' = d_2 \cdot \tan \xi_2$$

$$H''' = H - H' - H''$$

$$d_3 = \frac{H'''}{\tan \xi_3}$$

$$d = d_1 + d_2 + d_3$$

Appendix B

The size of the monochrome CMOS sensor utilized in the Scheimpflug lidar system was a 2448×2048 pixel array (approximately 5.0 megapixels, pixel size: $3.54 \mu\text{m} \times 3.54 \mu\text{m}$). A typical Scheimpflug lidar system has a lens (lens plane) and object planes that are not parallel and three planes that intersect at the Scheimpflug intersection line as Figure A1 shows. MN is a line on the object plane in the real-world coordinate system which represents the laser beam width at distance L , and $M'N'$ is the image of the line in the image coordinate system. O'' is the intersect point of the Scheimpflug lidar system. $O''M'$ is the theoretical centerline of the CMOS. $O''G'$ is the actual centerline of the CMOS. Thus, the $G'M'$ represents the distance between the centerline of the CMOS sensor and the laser beam. In addition, the relationship between MN and $M'N'$ is related to the distance and the pixel number. The relationship is illustrated in Figure 4. It is difficult to avoid the CMOS camera without a little displacement during the configuration. In our opinion, the slight displacement of the CMOS was the cause of the upward curvature in the laser beam width. Data gridding and

data interpolation were utilized during the data processing. Hence, the upward curvature in the laser beam width would not affect the results of laser beam width in the manuscript.

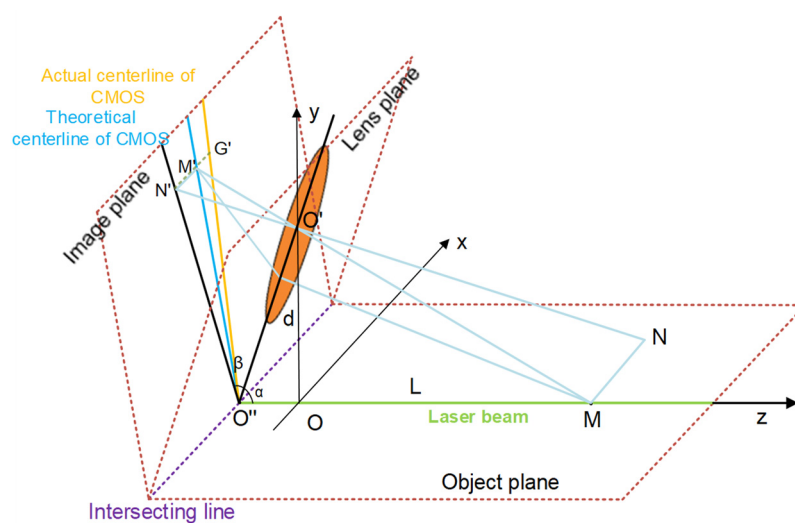


Figure A1. The relationship between the image and the real-world coordinate system. MN is a line on the object plane in the real-world coordinate system, and $M'N'$ is the image of the line in the image coordinate system. O'' is the intersect point of the Scheimpflug lidar system. $O''M'$ is the centerline of the CMOS in theory. $O'G'$ is the actual centerline of the CMOS.

Appendix C



Figure A2. Photograph of the river inside the campus of the Ocean University of China where we sampled the river water.

References

1. Soomets, T.; Uudeberg, K.; Jakovels, D.; Brauns, A.; Zagars, M.; Kutser, T. Validation and Comparison of Water Quality Products in Baltic Lakes Using Sentinel-2 MSI and Sentinel-3 OLCI Data. *Sensors* **2020**, *20*, 742. [[CrossRef](#)] [[PubMed](#)]
2. Aguilar-Maldonado, J.A.; Santamaría-del-Ángel, E.; Gonzalez-Silvera, A.; Sebastián-Frasquet, M.T. Detection of Phytoplankton Temporal Anomalies Based on Satellite Inherent Optical Properties: A Tool for Monitoring Phytoplankton Blooms. *Sensors* **2019**, *19*, 3339. [[CrossRef](#)]

3. Milton, K.; Joao, A.L.; Cristina, M.B. Simultaneous measurements of Chlorophyll concentration by lidar, fluorometry, above-water radiometry, and ocean color MODIS images in the Southwestern Atlantic. *Sensors* **2009**, *9*, 528–541. [[CrossRef](#)]
4. Michael, E.L.; Marlon, R.L. A new method for the measurement of the optical volume scattering function in the upper ocean. *J. Atmos. Ocean. Technol.* **2003**, *20*, 563–571. [[CrossRef](#)]
5. Eric, R.; Norman, J.M. Inherent optical property estimation in deep waters. *Opt. Express* **2011**, *19*, 24986–25005. [[CrossRef](#)]
6. David, R.L. Remote sensing of bottom reflectance and water attenuation parameters in shallow water using aircraft and Landsat data. *Int. J. Remote Sens.* **1981**, *2*, 71–82. [[CrossRef](#)]
7. Ina, L.; Fethi, B.; Charles, T.; Rüdiger, R.; David, B.; Alex, N.; Jill, S. Optical closure in marine waters from in situ inherent optical property measurements. *Opt. Express* **2016**, *24*, 14036–14052. [[CrossRef](#)]
8. Li, C.; Cao, W. An instrument for in-situ measuring the volume scattering function of water: Design, Calibration and Primary Experiments. *Sensors* **2012**, *12*, 4514–4533. [[CrossRef](#)]
9. Malik, C.; Richard, S.; Eric, D. Radiative transfer model for the computation of radiance and polarization in an ocean–atmosphere system: Polarization properties of suspended matter for remote sensing. *Appl. Opt.* **2001**, *40*, 2398–2416. [[CrossRef](#)]
10. Jin, Z.; Stamnes, K. Radiative transfer in nonuniformly refracting layered media: Atmosphere–ocean system. *Appl. Opt.* **1994**, *33*, 431–442. [[CrossRef](#)]
11. Gordon, H.R.; Wang, M. Retrieval of water-leaving radiance and aerosol optical thickness over the oceans with SeaWiFS: A preliminary algorithm. *Appl. Opt.* **1994**, *33*, 443–452. [[CrossRef](#)]
12. Massey, G.M.; Friedrichs, C.T. *Laser In-Situ Scattering and Transmissometer (LISST) Observations in Support of the Sensor Insertion System Duck, NC October 1997*; Data Report (Virginia Institute of Marine Science) no. 57; Virginia Institute of Marine Science, College of William and Mary, Commonwealth of Virginia: Gloucester Point, VA, USA, 1997. [[CrossRef](#)]
13. Doxaran, D.; Leymarie, E.; Nechad, B.; Dogliotti, A.; Ruddick, K.; Gernez, P.; Knaeps, E. Improved correction methods for field measurements of particulate light backscattering in turbid waters. *Opt. Express* **2016**, *24*, 3615–3637. [[CrossRef](#)]
14. Roesler, C.; Uitz, J.; Claustre, H.; Boss, E.; Xing, X.; Organelli, E.; Barbieux, M. Recommendations for obtaining unbiased chlorophyll estimates from in situ chlorophyll fluorometers: A global analysis of WET Labs ECO sensors. *Limnol. Oceanogr. Methods* **2017**, *15*, 572–585. [[CrossRef](#)]
15. Kim, H.; Lee, S.B.; Min, K.S. Shoreline change analysis using airborne LiDAR bathymetry for coastal monitoring. *J. Coast. Res.* **2017**, *79*, 269–273. [[CrossRef](#)]
16. Collister, B.L.; Zimmerman, R.C.; Sukenik, C.I.; Hill, V.J.; Balch, W.M. Remote sensing of optical characteristics and particle distributions of the upper ocean using shipboard lidar. *Remote Sens. Environ.* **2018**, *215*, 85–96. [[CrossRef](#)]
17. Behrenfeld, M.J.; Hu, Y.; O'Malley, R.T.; Boss, E.S.; Hostetler, C.A.; Siegel, D.A.; Sarmiento, J.L.; Schullien, J.; Hair, J.W.; Lu, X.; et al. Annual boom–bust cycles of polar phytoplankton biomass revealed by space-based lidar. *Nat. Geosci.* **2017**, *10*, 118–122. [[CrossRef](#)]
18. Wu, S.; Liu, B.; Liu, J.; Zhai, X.; Feng, C.; Wang, G.; Gallacher, D. Wind turbine wake visualization and characteristics analysis by Doppler lidar. *Opt. Express* **2016**, *24*, A762–A780. [[CrossRef](#)]
19. Zhai, X.; Wu, S.; Liu, B. Doppler lidar investigation of wind turbine wake characteristics and atmospheric turbulence under different surface roughness. *Opt. Express* **2017**, *25*, A515–A529. [[CrossRef](#)]
20. Zhang, H.; Wu, S.; Wang, Q.; Liu, B.; Yin, B.; Zhai, X. Airport low-level wind shear lidar observation at Beijing Capital International Airport. *Infrared Phys. Technol.* **2019**, *96*, 113–122. [[CrossRef](#)]
21. Dai, G.; Wu, S.; Song, X. Depolarization ratio profiles calibration and observations of aerosol and cloud in the Tibetan Plateau based on polarization Raman lidar. *Remote Sens.* **2018**, *10*, 378. [[CrossRef](#)]
22. Mei, L.; Brydegaard, M. Atmospheric aerosol monitoring by an elastic Scheimpflug lidar system. *Opt. Express* **2015**, *23*, A1613–A1628. [[CrossRef](#)]
23. Liu, Z.; Li, L.; Li, H. Preliminary Studies on Atmospheric Monitoring by Employing a Portable Unmanned Mie-Scattering Scheimpflug Lidar System. *Remote Sens.* **2019**, *11*, 837. [[CrossRef](#)]
24. Sun, G.; Qin, L.; Hou, Z.; Jing, X.; He, F. Small-scale Scheimpflug lidar for aerosol extinction coefficient and vertical atmospheric transmittance detection. *Opt. Express* **2018**, *26*, 7423–7436. [[CrossRef](#)]
25. Shaw, J.A.; Seldomridge, N.L.; Dunkle, D.L.; Nugent, P.W.; Spangler, L.H.; Bromenshenk, J.J.; Henderson, C.B.; Churnside, J.H.; Wilson, J.J. Polarization lidar measurements of honey bees in flight for locating land mines. *Opt. Express* **2005**, *13*, 5853–5863. [[CrossRef](#)]
26. Kirkeby, C.; Wellenreuther, M.; Brydegaard, M. Observations of movement dynamics of flying insects using high resolution lidar. *Sci. Rep.* **2016**, *6*, 29083. [[CrossRef](#)]
27. Tauc, M.J.; Fristrup, K.M.; Repasky, K.S.; Shaw, J.A. Field demonstration of a wing-beat modulation lidar for the 3D mapping of flying insects. *OSA Contin.* **2019**, *2*, 332–348. [[CrossRef](#)]
28. Li, Y.; Wang, K.; Quintero-Torres, R.; Brick, R.; Sokolov, A.V.; Scully, M.O. Insect flight velocity measurement with a CW near-IR Scheimpflug lidar system. *Opt. Express* **2020**, *28*, 21891–21902. [[CrossRef](#)]
29. Mei, L.; Kong, Z.; Guan, P. Implementation of a violet Scheimpflug lidar system for atmospheric aerosol studies. *Opt. Express* **2018**, *26*, A260–A274. [[CrossRef](#)]
30. Mei, L.; Brydegaard, M. Continuous-wave differential absorption lidar. *Laser Photonics Rev.* **2015**, *9*, 629–636. [[CrossRef](#)]

31. Mei, L.; Guan, P.; Kong, Z. Remote sensing of atmospheric NO₂ by employing the continuous-wave differential absorption lidar technique. *Opt. Express* **2017**, *25*, A953–A962. [[CrossRef](#)]
32. Lin, H.; Zhang, Y.; Mei, L. Fluorescence Scheimpflug LiDAR developed for the three-dimension profiling of plants. *Opt. Express* **2020**, *28*, 9269–9279. [[CrossRef](#)] [[PubMed](#)]
33. Gordon, H.R. Interpretation of airborne oceanic lidar: Effects of multiple scattering. *Appl. Opt.* **1982**, *21*, 2996–3001. [[CrossRef](#)] [[PubMed](#)]
34. Walker, R.E.; McLean, J.W. Lidar equations for turbid media with pulse stretching. *Appl. Opt.* **1999**, *38*, 2384–2397. [[CrossRef](#)] [[PubMed](#)]
35. Roddewig, M.R.; Churnside, J.H.; Shaw, J.A. Lidar measurements of the diffuse attenuation coefficient in Yellow Lake. *Appl. Opt.* **2020**, *59*, 3097–3101. [[CrossRef](#)]
36. Bogucki, D.J.; Piskozub, J.; Carr, M.E.; Spiers, G.D. Monte Carlo simulation of propagation of a short light beam through turbulent oceanic flow. *Opt. Express* **2007**, *15*, 13988–13996. [[CrossRef](#)]
37. Liu, D.; Xu, P.; Zhou, Y.; Chen, W.; Han, B.; Zhu, X.; Chen, S. Lidar remote sensing of seawater optical properties: Experiment and Monte Carlo simulation. *IEEE Trans. Geosci. Remote Sens.* **2019**, *57*, 9489–9498. [[CrossRef](#)]
38. Poole, L.R.; Venable, D.D.; Campbell, J.W. Semianalytic Monte Carlo radiative transfer model for oceanographic lidar systems. *Appl. Opt.* **1981**, *20*, 3653–3656. [[CrossRef](#)]
39. Churnside, J.H. Review of profiling oceanographic lidar. *Opt. Eng.* **2014**, *53*, 051405. [[CrossRef](#)]
40. Morel, A.; Prieur, P. Analysis of variations in ocean color. *Limnol. Oceanogr.* **1997**, *22*, 709–722. [[CrossRef](#)]
41. Gordon, H.R.; Morel, A. Remote assessment of ocean color for interpretation of satellite visible imagery: A review. In *Lecture Notes on Coastal and Estuarine Studies*; Springer: New York, NY, USA, 1983.
42. Petzold, T.J. *Volume Scattering Functions for Selected Ocean Waters*; Naval Air Development Center: Warminster, PA, USA, 1972.
43. Sassen, K.; Zhu, J.; Webley, P.; Dean, K.; Cobb, P. Volcanic ash plume identification using polarization lidar: Augustine eruption, Alaska. *Geophys. Res. Lett.* **2007**, *34*. [[CrossRef](#)]